



Probing the Heights and Depths of Y Dwarf Atmospheres: A Retrieval Analysis of the JWST Spectral Energy Distribution of WISE J035934.06–540154.6

Harshil Kothari¹ , Michael C. Cushing¹ , Ben Burningham² , Samuel A. Beiler¹ , J. Davy Kirkpatrick³ ,
Adam C. Schneider⁴ , Sagnick Mukherjee⁵ , and Mark S. Marley⁶

¹Ritter Astrophysical Research Center, Department of Physics & Astronomy, University of Toledo, 2801 W. Bancroft Street, Toledo, OH 43606, USA

²Centre for Astrophysics Research, School of Physics, Astronomy and Mathematics, University of Hertfordshire, Hatfield AL10 9AB, UK

³IPAC, Mail Code 100-22, Caltech, 1200 E. California Boulevard, Pasadena, CA 91125, USA

⁴United States Naval Observatory, Flagstaff Station, 10391 West Naval Observatory Road, Flagstaff, AZ 86005, USA

⁵Department of Astronomy and Astrophysics, University of California, Santa Cruz, 1156 High Street, Santa Cruz, CA 95064, USA

⁶Lunar and Planetary Laboratory, University of Arizona, 1629 E. University Boulevard, Tucson, AZ 85721, USA

Received 2024 April 16; revised 2024 May 24; accepted 2024 June 10; published 2024 August 12

Abstract

We present an atmospheric retrieval analysis of the Y0 brown dwarf WISE J035934.06–540154.6 using the low-resolution 0.96–12 μm James Webb Space Telescope (JWST) spectrum presented in Beiler et al. We obtain volume number mixing ratios of the major gas-phase absorbers (H_2O , CH_4 , CO , CO_2 , PH_3 , and H_2S) that are three to five times more precise than previous work that used Hubble Space Telescope (HST) spectra. We also find an order-of-magnitude improvement in the precision of the retrieved thermal profile, a direct result of the broad wavelength coverage of the JWST data. We used the retrieved thermal profile and surface gravity to generate a grid of chemical forward models with varying metallicity, $(\text{C}/\text{O})_{\text{atm}}$, and strengths of vertical mixing as encapsulated by the eddy diffusion coefficient K_{zz} . Comparison of the retrieved abundances with this grid of models suggests that the deep atmosphere of WISE 0359–54 shows signs of vigorous vertical mixing with $K_{zz} = 10^9 \text{ cm}^2 \text{ s}^{-1}$. To test the sensitivity of these results to our five-knot spline thermal profile model, we performed a second retrieval using the Madhusudhan & Seager thermal profile model. While the results of the two retrievals generally agree well, we do find differences between the retrieved values of mass and volume number mixing ratio of H_2S with fractional differences of the median values of -0.64 and -0.10 , respectively. In addition, the five-knot thermal profile is consistently warmer at pressure between 1 and 70 bar. Nevertheless, our results underscore the power that the broad-wavelength infrared spectra obtainable with the JWST have to characterize the atmospheres of cool brown dwarfs.

Unified Astronomy Thesaurus concepts: [Stellar abundances \(1577\)](#); [Stellar atmospheres \(1584\)](#); [Atmospheric structure \(2309\)](#); [Brown dwarfs \(185\)](#); [Bayesian statistics \(1900\)](#); [Radiative transfer \(1335\)](#)

1. Introduction

In the last decade, atmospheric retrieval, a method by which the properties of an atmosphere are inferred directly from an observed spectrum, has become a powerful technique for studying the atmospheres of both brown dwarfs and exoplanets (e.g., Madhusudhan & Seager 2009; Line et al. 2014). With roots in the study of the planets in our solar system (e.g., Chahine 1968), a retrieval determines the thermal profile (i.e., the run of temperature and pressure) and atomic/molecular abundances of an atmosphere by iteratively comparing tens of thousands of model spectra to observations in order to optimize the model parameters.

Previous retrievals of brown dwarfs have mostly focused on the warmer objects that populate the L and T spectral classes (Line et al. 2014; Burningham et al. 2017; Zalesky et al. 2019; Lueber et al. 2022; Adams et al. 2023; Rowland et al. 2023; Vos et al. 2023; Hood et al. 2024). These retrievals use relatively broad-wavelength spectra covering a minimum of the 0.8–2.4 μm wavelength and often extending to 4–5 μm or even to $\sim 15 \mu\text{m}$.

The cooler brown dwarfs that populate the Y spectral class are rare (roughly 50 are known), faint ($M_H \gtrsim 21 \text{ mag}$), and emit most of their radiation at mid-infrared wavelengths. As a result, the majority of retrievals that have been performed on them used spectra with limited wavelength coverage and/or signal-to-noise ratio. Zalesky et al. (2019) performed retrievals of eight Y dwarfs using low-resolution 1–1.7 μm Hubble Space Telescope (HST) spectra (Schneider et al. 2015) and measured the abundances of H_2O , CH_4 , NH_3 , and upper limits for the abundances of CO and CO_2 . The H_2O and CH_4 abundances were consistent with the predictions of thermochemical equilibrium models, but Zalesky et al. suggested that the abundance of NH_3 may be affected by vertical mixing within the atmosphere. Unfortunately, the narrow wavelength coverage of the HST spectra limits the precision with which the abundances and the thermal profiles can be measured (uncertainties of $\sim 0.14 \text{ dex}$ and $\sim 200 \text{ K}$, respectively) because they only probe a relatively narrow range of pressures in the atmosphere.

The launch of the James Webb Space Telescope (hereafter JWST; Gardner et al. 2006) has opened a new frontier in the study of Y dwarfs because low- and moderate-resolution spectra are now available over the 1 to 28 μm wavelength range. Barrado et al. (2023) used several retrieval codes to detect both $^{14}\text{NH}_3$ and $^{15}\text{NH}_3$ in the moderate-resolution 4.9–18 μm spectrum of WISEP J182831.08+265037.8



Original content from this work may be used under the terms of the [Creative Commons Attribution 4.0 licence](#). Any further distribution of this work must maintain attribution to the author(s) and the title of the work, journal citation and DOI.

(hereafter WISE 1828+25; $T_{\text{eff}} \approx 350$ K) and found a $^{14}\text{N}/^{15}\text{N}$ value of 673_{-212}^{+393} , consistent with formation by gravitational collapse of a molecular cloud. Lew et al. (2024) used a moderate-resolution 2.88–5.12 μm spectrum of WISE 1828+26 to obtain abundances of H_2O , CH_4 , CO_2 , NH_3 , and H_2S , and measured a C/O value of 0.45 ± 0.01 .

In this paper, we add to the short list of brown dwarf JWST-based retrievals by presenting a retrieval analysis of WISE J035934.06–540154.6 (hereafter WISE 0359–54) using the low-resolution 0.96–12 μm JWST spectrum presented in Beiler et al. (2023). WISE 0359–54 has a spectral type of Y0, lies at a distance of 13.57 ± 0.37 pc ($\varpi_{\text{abs}} = 73.6 \pm 2.0$ mas, Kirkpatrick et al. 2021), and has an effective temperature (T_{eff}) of 467_{-18}^{+16} K (Beiler et al. 2023). In Section 2, we will briefly discuss the spectrum being used for this analysis. In Section 3, we will discuss the retrieval framework that is used to perform the retrieval analysis for WISE 0359–54. In Section 4, we will present and discuss the retrieved results. Finally, in Section 5, we will summarize and point out the key findings of this retrieval analysis.

2. The Spectrum

We analyzed the 0.96–12 μm JWST spectrum of the Y0 dwarf WISE 0359–54 presented in Beiler et al. (2023). The spectrum was obtained using the Near Infrared Spectrograph (hereafter NIRSpec; Jakobsen et al. 2022), which covers 0.6–5.3 μm , and the Mid-Infrared Instrument (hereafter MIRI; Rieke et al. 2015), which covers 5–12 μm . The resolving power of the spectra is a strong function of wavelength but on average is $R \equiv \lambda/\Delta\lambda \approx 200$. Beiler et al. (2023) used Spitzer/IRAC Channel 2 ([4.5]) photometry from Kirkpatrick et al. (2012) and MIRI F1000W ($\lambda_{\text{pivot}} = 9.954$ μm) photometry to absolutely flux calibrate the NIRSpec and MIRI spectra to an overall precision of $\sim 5\%$. Beiler et al. (2023) then created a continuous 0.96–12 μm spectrum by merging the NIRSpec and the MIRI spectrum between 5 and 5.3 μm , where the spectra overlapped. The 0.96–12 μm spectrum is shown in Figure 1 in units of f_λ along with the locations of prominent molecular absorption bands of H_2O , CH_4 , CO , CO_2 , and NH_3 identified by Beiler et al. (2023).

3. The Method

We use the Brewster retrieval framework (Burningham et al. 2017) for our analysis. We assume that each datum in the spectrum is generated from the following probabilistic model:

$$F_\lambda(\lambda_i) = (R/d)^2 [\mathbf{I}(\lambda_i) * \mathcal{F}_\lambda(\boldsymbol{\theta}_{\text{atm}}, \lambda_j)] + \epsilon(\lambda_i), \quad (1)$$

where $F_\lambda(\lambda_i)$ is a random variable giving the flux density of the spectrum at the i th wavelength λ_i , R is the radius of the brown dwarf, d is the distance of the brown dwarf, $\mathbf{I}(\lambda_i)$ is the instrument profile at λ_i , the asterisk denotes a convolution, \mathcal{F}_λ is a model emergent flux density at the surface of the brown dwarf, $\boldsymbol{\theta}_{\text{atm}}$ is a vector of parameters describing the atmospheric model, λ_j is equal to $\lambda_k + \Delta\lambda$, where λ_k is the wavelength at which the model emergent flux is calculated and $\Delta\lambda$ is a parameter that accounts for any wavelength uncertainty, and $\epsilon(\lambda_i)$ is a random variable that is distributed as a Gaussian with a mean of zero and a variance of $\sigma(\lambda_i)^2$. We further assume the

variances $\sigma^2(\lambda_i)$ are given by

$$\sigma^2(\lambda_i) = s^2(\lambda_i) + 10^b, \quad (2)$$

where $s(\lambda_i)$ is the standard error of the spectrum at λ_i and b is a tolerance parameter that is used to inflate the measured uncertainties to account for unaccounted sources of uncertainty (e.g., Hogg et al. 2010; Foreman-Mackey et al. 2013; Burningham et al. 2017).

The one-dimensional atmospheric model is divided into 64 layers (65 levels), with the pressure ranging from 10^{-4} to $10^{2.3}$ bar, in steps of 0.1 dex. This range was chosen based on the pressure regions that can be probed with the spectrum being used for this retrieval analysis and the available opacities. For simplicity we assume the atmosphere is cloudless and so the only sources of opacity are the absorbing gases H_2 , He, H_2O , CH_4 , CO , CO_2 , NH_3 , H_2S , K, Na, and PH_3 . H_2 and He contribute a continuum opacity in the form of collision-induced absorption (i.e., $\text{H}_2\text{--H}_2$, $\text{H}_2\text{--CH}_4$, and $\text{H}_2\text{--He}$). The uniform-with-altitude volume number mixing ratios⁷ (hereafter mixing ratios) of the remaining molecules are free parameters. The thermal profile is modeled with a five-knot interpolating spline in which the knots are located at the top (T_{Knot1}), middle (T_{Knot3}), and bottom (T_{Knot5}) of the atmosphere, with one point halfway between the top and the middle (T_{Knot2}) of the atmosphere, and one point halfway between the bottom and the middle (T_{Knot4}) of the atmosphere. The mass and radius of the brown dwarf are also free parameters, which are then used to calculate the surface gravity ($g = GM/R^2$). Taken together, the parameters for the mixing ratios of the nine gas species, the five parameters for the thermal profile, and mass and radius make up $\boldsymbol{\theta}_{\text{atm}}$ in Equation (1).

For a given $\boldsymbol{\theta}_{\text{atm}}$, the emergent spectrum at the top of the atmospheric \mathcal{F}_λ is calculated by using a two-stream source function technique from Toon et al. (1989). The emergent spectrum is then convolved with the instrument profile $\mathbf{I}(\lambda_i)$, which we assume is a Gaussian, to account for the variable resolving power of the data (see Beiler et al. (2023) for further discussion on this latter process).

If we let $\boldsymbol{\Theta} = \{\boldsymbol{\theta}_{\text{atm}}, d, b, \Delta\lambda\}$, then we can use Bayes' theorem to calculate the posterior probability density function for the parameters $\boldsymbol{\Theta}$ given the data \mathbf{f}_λ ,

$$p(\boldsymbol{\Theta}|\mathbf{f}_\lambda) = \frac{p(\boldsymbol{\Theta})\mathcal{L}(\mathbf{f}_\lambda|\boldsymbol{\Theta})}{p(\mathbf{f}_\lambda)}, \quad (3)$$

where $p(\boldsymbol{\Theta})$ is the prior probability for the set of parameters, $\mathcal{L}(\mathbf{f}_\lambda|\boldsymbol{\Theta})$ is the likelihood that quantifies the probability of the data given the model, and $p(\mathbf{f}_\lambda)$ is the Bayesian evidence. If we let

$$\mathcal{M}_\lambda(\lambda_i) = (R/d)^2 [\mathbf{I}(\lambda_i) * \mathcal{F}_\lambda(\boldsymbol{\theta}_{\text{atm}}, \lambda_j)], \quad (4)$$

then the natural logarithm of the likelihood function is given by

$$\ln \mathcal{L}(\mathbf{f}_\lambda|\boldsymbol{\Theta}) = -\frac{1}{2} \sum_{i=1}^n \left\{ \frac{[f_{\lambda,i} - \mathcal{M}_\lambda(\lambda_i)]^2}{\sigma(\lambda_i)^2} - \ln[2\pi\sigma(\lambda_i)^2] \right\} \quad (5)$$

⁷ The volume number mixing ratio of a species is the number density of that species divided by the total number density of the gas.

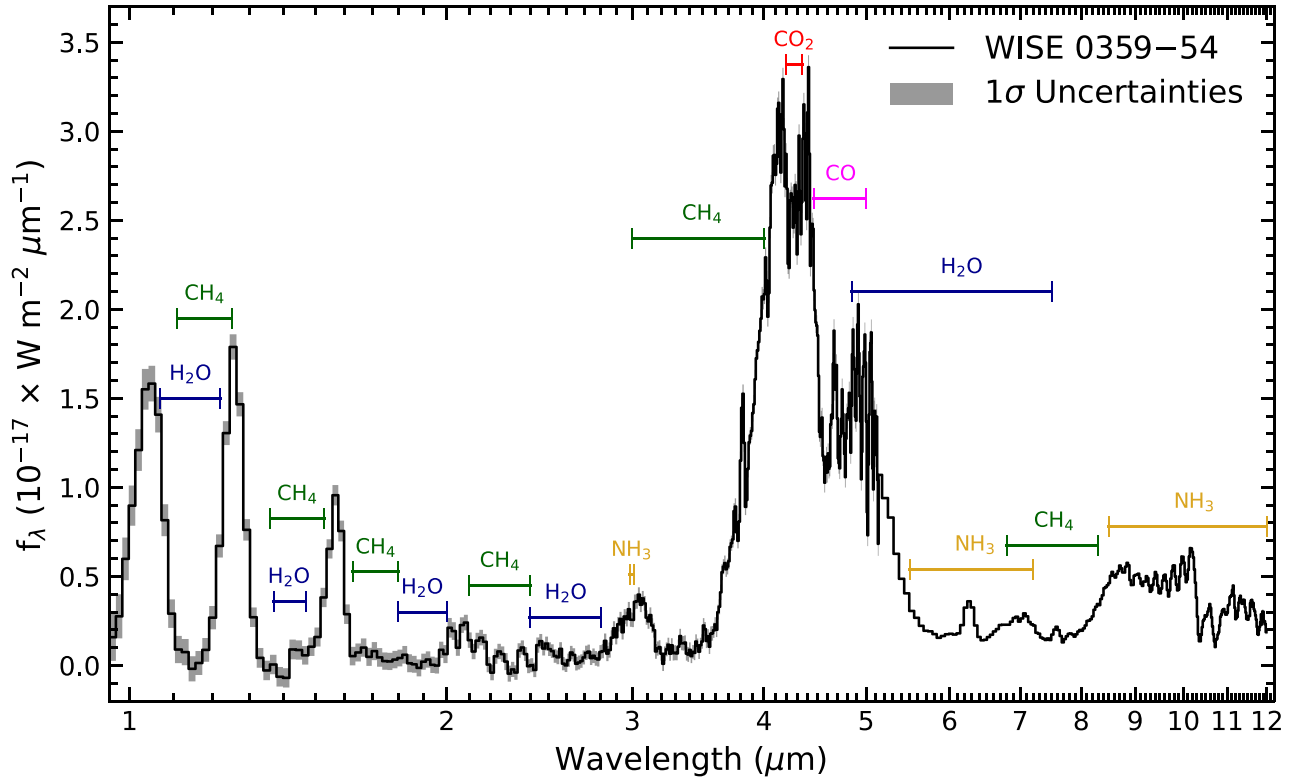


Figure 1. The 0.96–12 μm JWST spectrum with 1σ uncertainties (NIRSpec + MIRI low-resolution spectrometer (LRS)) of WISE 0359–54 spectrum (Beiler et al. 2023) in units of f_λ . The typical signal-to-noise of the NIRSpec and MIRI LRS spectra are ~ 20 and ~ 100 , respectively. Also plotted are the locations of prominent absorption bands of H_2O , CH_4 , CO , CO_2 , and NH_3 .

Table 1
Parameters Priors

Parameter	Prior ^a
Gas Volume Mixing Ratio $\log(f_i)$ ^{b,c}	$\mathcal{U}(-12, \infty)$, $\sum_{i=1}^9 f_i \leq 1$
Mass M ($\mathcal{M}_{\text{Jup}}^N$)	$\mathcal{U}(1, 80)$
Radius R (\mathcal{R}_{J}^N)	$\mathcal{U}(0.5, 2)$
Wavelength Shift $\Delta\lambda$ (μm)	$\mathcal{U}(-0.01, 0.01)$
Tolerance Factor b	$\mathcal{U}(10^{0.01} \times \min(\sigma_i^2), 10^{100} \times \max(\sigma_i^2))$
Five-knot Thermal Profile: $T_{\text{Knot } i}(\text{K})$	$\mathcal{U}(0, 5000)$
Madhusudhan & Seager Thermal Profile: $\alpha_1, \alpha_2, P_1, P_3, T_3$	$\mathcal{U}(0.25, 0.5)$, $\mathcal{U}(0.1, 0.2)$, $\mathcal{U}(10^{-4}, 10^{2.3})$, $\mathcal{U}(10^{-4}, 10^{2.3})$, $\mathcal{U}(0, 5000)$
Distance d (pc)	$\mathcal{N}(13.57, 0.37^2)$

Note.

^a $\mathcal{U}(\alpha, \beta)$ denotes a uniform distribution between α and β while $\mathcal{N}(\mu, \sigma^2)$ denotes a normal distribution with a mean of μ and a variance of σ^2 .

^b We included H_2O , CH_4 , CO , CO_2 , NH_3 , H_2S , K , Na , and PH_3 .

^c All volume mixing ratios are reported as the log of the volume number mixing ratio (the number density of the species divided by the total number density of the gas), where the remainder of the gas is assumed to be H_2 -He ($1 - \sum_i f_i$). Of the remainder of the gas, 84% of the volume mixing ratio is from H_2 and 16% is from He, assuming a solar abundance of 91.2% of the number of atoms of H and 8.7% of the number of atoms of He (Asplund et al. 2009).

because we assume that the data are independent and $\epsilon(\lambda)$ is distributed as a Gaussian. The prior distributions for each of the 19 parameters are given in Table 1.

To explore the posterior parameter space, we use the nested sampling version of the `Brewster`, which uses `PyMultiNest` (Buchner et al. 2014). `PyMultiNest` is initialized to sample the parameter space with 500 live points for 19 free parameters. The calculation was done using the Owens cluster (Center 2016) at the Ohio Supercomputer Center (Center 1987). The sampling is complete when the change in the natural logarithm

of the evidence is less than 0.5 (for a deeper discussion, see Feroz et al. 2009; Speagle 2020).

4. Results and Discussion

The result of solving Bayes' theorem is a joint posterior distribution for the 19 parameters. In the Appendix, Figure 12 shows the marginalized posterior probability distributions for all 19 parameters using equally weighted posterior samples generated by `PyMultiNest` and Table 3 gives the median,

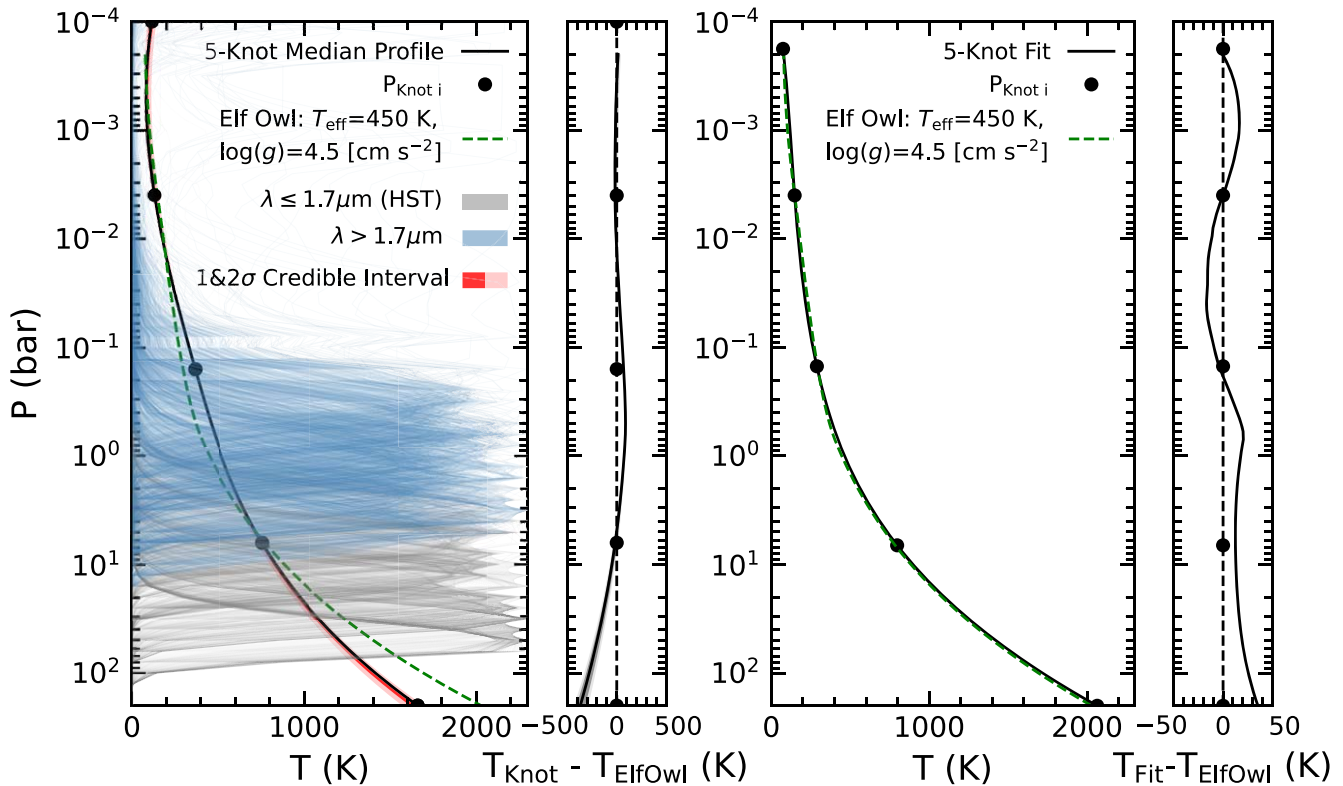


Figure 2. Left two panels (retrieved vs. forward model): the black solid curve shows the five-knot retrieved median thermal profile, the red region shows the 1σ and 2σ central credible interval around the median profile, and the green dashed curve is a solar metallicity, solar C/O ratio, and cloudless Elf Owl thermal profile with $T_{\text{eff}} = 450$ K and $\log(g) = 4.5$ [cm s^{-2}]. Also plotted are normalized contribution functions in gray (HST wavelength coverage, $\lambda \leq 1.7 \mu\text{m}$) and in blue ($\lambda > 1.7 \mu\text{m}$). The handful of contributions functions at pressure lower than 10^{-2} bar come primarily from the 6.3–7.8 μm wavelength range. Right two panels (forward model vs. forward model fit): the dashed green curve is the Elf Owl thermal profile with a $T_{\text{eff}} = 450$ K and $\log(g) = 4.5 \text{ cm s}^{-2}$ and the black solid curve shows the five-knot spline fit of the same Elf Owl thermal profile. The black dots in all the panels represent the position of the five knots. Note: The temperature range in panel (2) is an order of magnitude larger than the range in panel (4).

and 1σ uncertainty for each of the parameters. In the following sections, we discuss the values of these parameters in more detail.

4.1. The Thermal Profile

The first panel in Figure 2 shows the retrieved thermal profile; the black solid line shows the median (50th percentile) profile (calculated using the median values of the retrieved parameters) and the red shaded region represents the 16th and 84th percentiles (1σ central credible interval),⁸ and 2.4th and 97.6th percentiles (2σ central credible interval). Also plotted is a subset of normalized contribution functions at wavelengths covering the 0.96–12 μm wavelength range; those in gray are the wavelengths covered by HST/WFC3 spectra ($\lambda < 1.7 \mu\text{m}$) while the blue cover the wavelengths longward of 1.7 μm . Integration of a contribution function over (log) pressure in a semi-infinite atmosphere gives the specific intensity at the top of the atmosphere at the corresponding wavelength (Chamberlain & Hunten 1987). A normalized contribution function therefore indicates the layers of the atmospheres from which light at that wavelength emerges. The opacity windows centered at the *J* and *H* bands probe deep, hotter layers of

the atmosphere (gray lines), while longer wavelengths generally probe higher and cooler layers of the atmosphere (blue lines). The handful of contributions functions at pressure lower than 10^{-2} bar come primarily from the 6.3–7.8 μm wavelength range. The JWST spectrum therefore probes nearly 4 orders of magnitude in pressure; two more than previous work (Zalesky et al. 2019) using HST spectra alone. In addition, the median width of the 1σ central credible interval is ~ 20 K, which is an order of magnitude lower than typically found using HST spectra alone (Zalesky et al. 2019).

A cloudless self-consistent 1D radiative-convective equilibrium Sonora Elf Owl thermal profile with solar metallicity and C/O ratio (green dashed line; Mukherjee et al. 2024) is also plotted in the first panel of Figure 2. The effective temperature and (log) surface gravity of 450 K and 4.5 [cm s^{-2}] were chosen to match our derived values of 458 K and 4.46 [cm s^{-2}] (see Section 4.4) as closely as possible. The difference between the two profiles is shown in the second panel of Figure 2. Overall, the retrieved profile matches the self-consistent profile well, although the retrieved profile is systematically hotter by up to 100 K between 0.01 and 10 bars and systematically cooler by up to 500 K in the deepest layers of the atmosphere. The retrieved profile also shows a slight temperature reversal of ~ 30 K at the top of the atmosphere. While this is probably unphysical, Faherty et al. (2024) did identify CH_4 emission in the moderate-resolution JWST spectrum of the Y dwarf CWISEP J193518.59–154620.3 at 3.326 μm . They modeled

⁸ A Bayesian central credible interval gives the range of values in a parameter’s posterior distribution that contains $\alpha\%$ of the probability. In contrast, a frequentist $\alpha\%$ confidence interval means that $\alpha\%$ of a large number of confidence intervals computed in the same way would contain the true value of the parameter.

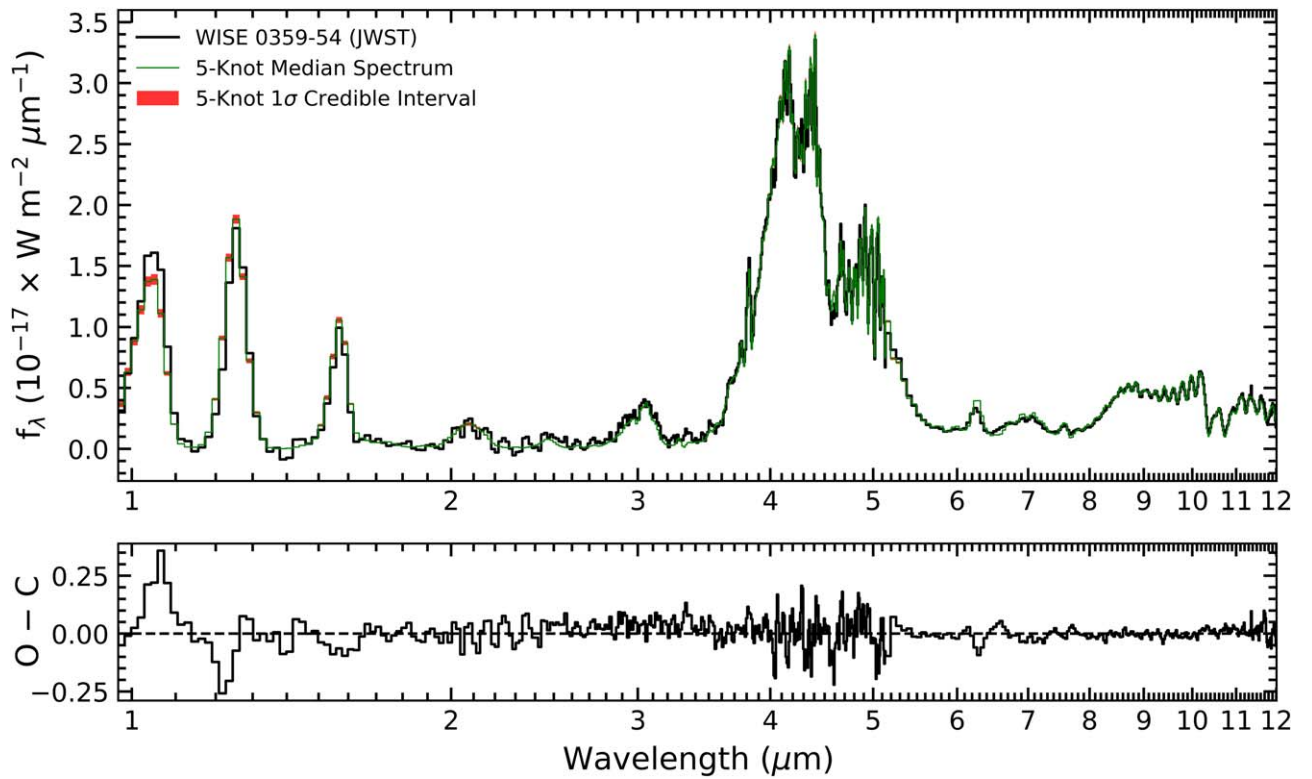


Figure 3. The top panel shows the observed spectrum in black and the retrieved median spectrum from five-knot retrieval in green for WISE 0359–54 spectrum covering 0.96–12 μm . The red region shows the 1σ central credible interval around the median spectrum. The bottom panel shows the residual spectrum calculated by taking the difference between the retrieved median spectrum and the observed spectrum.

this as a 300 K temperature reversal between the 1 and 10 mbar pressure range and so further investigation into our reversal is warranted.

In order to investigate the possibility that the differences between the retrieved profile and the Elf Owl profile are due to an inability of the five-knot spline to reproduce the shape of the Elf Owl profile, we have fitted the Elf Owl profile with a five-knot spline and the results are shown in the third panel of Figure 2; the difference between the two profiles is shown in the last panel. The Elf Owl profile does not extend up to the 10^{-4} bar level so we placed the top knot at $10^{-3.7}$ bar, the vertical extent of the Elf Owl profile. The five-knot spline easily reproduces the Elf Owl profile with a root mean squared deviation of 17 K and a maximum deviation of <50 K. This indicates that the differences between the retrieved profile and the Elf Owl profile are real and statistically significant.

4.2. Retrieved Model Spectrum

Figure 3 shows the JWST spectrum of WISE 0359–54 along with the retrieved median model spectrum (upper panel) and the residual ($O-C$, lower panel). The model spectrum is generated using the median thermal profile and the 1σ central credible interval is generated using the 1σ of the five-knot thermal profile. Overall, the model fits the data well as the residuals are mostly random. However, the model fails to reproduce the observations in the 1–2 μm range. The poor agreement shortward of 1.1 μm is likely a result of our poor understanding of the exact shape of the pressure-broadened wings of the resonant KI and NaI doublets at 7665/7699 Å and 8183/8195 Å, respectively (see Burningham et al. (2017) for a more in-depth discussion).

4.3. Mixing Ratios

Figure 4 shows the marginalized posterior probability distributions for the mixing ratios of H_2O , CH_4 , CO , CO_2 , NH_3 , and H_2S . With secure detections of all the dominant carbon- and oxygen-bearing molecules, we can also calculate the atmospheric $(\text{C}/\text{O})_{\text{atm}}$ ratio as

$$(\text{C}/\text{O})_{\text{atm}} = \frac{f_{\text{CO}} + f_{\text{CO}_2} + f_{\text{CH}_4}}{f_{\text{H}_2\text{O}} + f_{\text{CO}} + 2f_{\text{CO}_2}}, \quad (6)$$

and so Figure 4 also shows the marginalized posterior probability distribution for $(\text{C}/\text{O})_{\text{atm}}$ calculated using the samples of f_{CO} , f_{CO_2} , f_{CH_4} , and $f_{\text{H}_2\text{O}}$. It should be noted that $\sim 20\%$ of oxygen is depleted due to the sequestration of oxygen in condensates like enstatite (MgSiO_3) and forsterite (MgSi_2O_4) (Lodders & Fegley 2002), which would bring the median bulk $(\text{C}/\text{O})_{\text{bulk}}$ to 0.455, calculated using the method from Calamari et al. (2024).

In order to perform a sanity check on our retrieved abundances and $(\text{C}/\text{O})_{\text{atm}}$ ratio, we compare our values to those reported by Zalesky et al. (2019) for eight Y dwarfs, and Barrado et al. (2023) and Lew et al. (2024) for the archetype Y dwarf WISE 1828+26 in Table 2. We note that the Barrado et al. uncertainties are an order of magnitude larger than the other works because they were computed by combining (with equal weight) the posterior distributions from five different retrieval analyses.

In general, the mixing ratio and $(\text{C}/\text{O})_{\text{atm}}$ values agree well. The mixing ratios of H_2O and NH_3 fall within the range of values found by Zalesky et al. (2019) but the values for CH_4 and $(\text{C}/\text{O})_{\text{atm}}$ fall toward the lower and upper limits of the

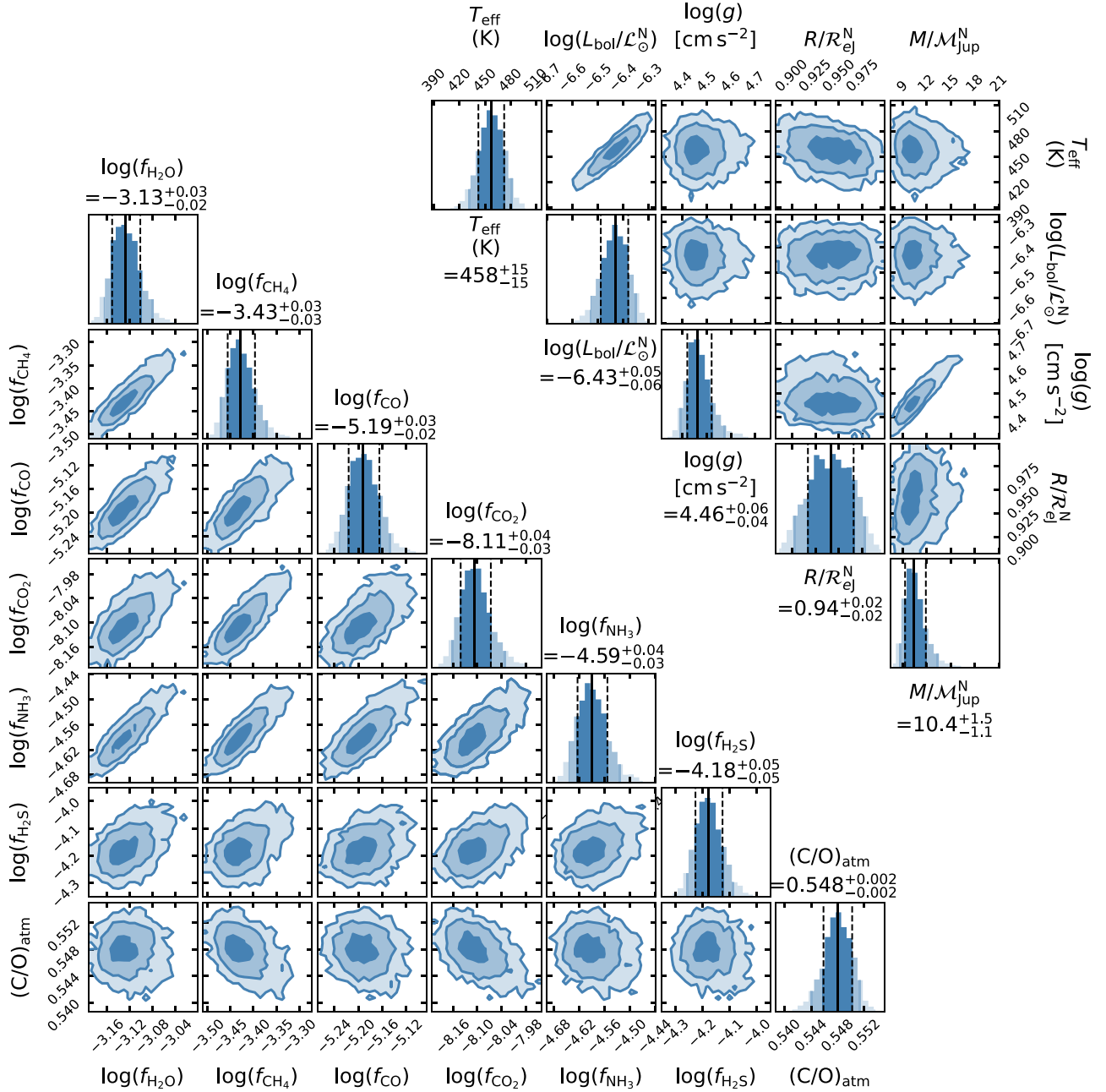


Figure 4. Lower left: marginalized posterior probability distributions for H_2O , CH_4 , CO , CO_2 , NH_3 , H_2S , and atmospheric $(\text{C/O})_{\text{atm}}$ from the five-knot retrieval for WISE 0359–54. Upper right: marginalized posterior probability distributions for T_{eff} , L_{bol} , $\log(g)$, R_{ej}^{N} , and $M_{\text{Jup}}^{\text{N}}$ from the five-knot retrieval for WISE 0359–54. In both panels, the values above the histograms represent the parametric median (50th percentile) values with the errors representing the 1σ (16th and 84th percentiles) values. The different shades in the 1D and 2D histograms represent the 1σ , 2σ , and 3σ central credible intervals, respectively, with the darkest shade corresponding to 1σ .

ranges, respectively. Our values and those of Lew et al. (2024) are inconsistent given the uncertainties; however, this could be because WISE 1828+26 is 110 K cooler than WISE 0359–54 and/or because both sets of measurements are likely dominated by systematic uncertainties not accounted for in the respective analyses (see Section 4.6). The Barrado et al. values generally agree with our values, but this is more likely a result of their order of magnitude larger uncertainties generated by combining the results of several retrieval analyses.

H_2S exhibits many rotation-vibrational bands in the 1–12 μm wavelength range centered at 1.33, 1.6, 2, 2.6, 4.0, and 8.0 μm . However, with the exception of a single absorption line

detected at $\lambda = 1.590 \mu\text{m}$ in an $R \approx 45,000$ spectrum of the T6 dwarf Two Micron All Sky Survey J08173001–6155158 (Tannock et al. 2022), spectral features of H_2S have remained undetected in the spectra of cool brown dwarfs. However, Hood et al. (2023) showed that a retrieval that includes H_2S as an opacity source produced a better fit to the moderate-resolution ($R \sim 6000$) near-infrared spectrum of the T9 dwarf UGPS J072227.51–054031.2 than a retrieval without H_2S opacity. Lew et al. also found that excluding H_2S opacity in their retrieval of WISE 1828+26 increased the χ^2 of the fit by over 900. These results suggest that retrievals can still detect H_2S in the atmospheres of cool brown dwarfs even though

Table 2
Parametric Value Comparison

Parameter	W0359–54		Eight Y Dwarfs	WISE J1828+26	
	This Work			Zalesky et al. (2019) (min–max)	Lew et al. (2024)
	Five Knot	Parametrized			
$\log(f_{\text{H}_2\text{O}})$	$-3.13^{+0.03}_{-0.02}$	$-3.10^{+0.04}_{-0.04}$	–2.68–3.32	$-2.71^{+0.01}_{-0.02}$	$-3.03^{+0.18}_{-0.21}$
$\log(f_{\text{CH}_4})$	$-3.43^{+0.03}_{-0.03}$	$-3.34^{+0.04}_{-0.04}$	–2.63–3.42	$-3.07^{+0.01}_{-0.02}$	$-3.65^{+0.11}_{-0.21}$
$\log(f_{\text{CO}})$	$-5.19^{+0.03}_{-0.02}$	$-5.18^{+0.04}_{-0.04}$	–3.3–4.2 ^b
$\log(f_{\text{CO}_2})$	$-8.11^{+0.04}_{-0.03}$	$-8.05^{+0.05}_{-0.05}$	–3.6–4.6 ^b	$-8.79^{+0.03}_{-0.04}$...
$\log(f_{\text{NH}_3})$	$-4.59^{+0.04}_{-0.03}$	$-4.51^{+0.05}_{-0.05}$	–4.11–4.84	$-4.21^{+0.02}_{-0.02}$	$-4.79^{+0.15}_{-0.25}$
$\log(f_{\text{H}_2\text{S}})$	$-4.18^{+0.05}_{-0.05}$	$-4.60^{+0.12}_{-0.12}$	–4.3–6.3 ^b	$-4.44^{+0.03}_{-0.03}$...
C/O	$0.548^{+0.002}_{-0.002}$	$0.538^{+0.003}_{-0.002}$	–0.55–1.10	$0.45^{+0.01}_{-0.01}$	$0.21^{+0.45}_{-0.03}$

Notes.

^a Averaged retrieved results from five different retrieval codes.

^b These ranges represent 3σ upper limit values.

there are no obvious absorption features in their low- to moderate-resolution spectra. Lew et al. retrieved a mixing ratio of $-4.44^{+0.03}_{-0.03}$ for WISE 1828+26, which is 0.24 dex lower than our value. We note that these are the only two detections of H₂S in atmospheres of Y dwarfs and so a larger sample of cool brown dwarfs will be required (H. Kothari et al., 2024, in preparation) to determine whether this difference is significant or not.

Finally, we included PH₃ as a source of opacity in our retrieval because the best-fitting Sonora model for WISE 0359–54 in Beiler et al. (2023) predicts the presence of phosphine. However, our retrieved mixing ratio of $-10.00^{+1.15}_{-1.26}$ is consistent with the lack of any PH₃ spectroscopic features (Beiler et al. 2023). The lack of PH₃ absorption bands in the spectra of the coolest brown dwarfs (down to ~ 250 K) (Miles et al. 2020; Luhman et al. 2024) remains an outstanding problem given that PH₃ has been detected in the spectra of Jupiter and Saturn (Gillett et al. 1973; Beer 1975; Bregman et al. 1975; Barshay & Lewis 1978).

Figure 5 shows a comparison of the mixing ratios for H₂O, CH₄, CO, CO₂, NH₃, and H₂S to the predictions of a thermochemical equilibrium model. The solid colored bars indicate the 1σ central credible interval for each mixing ratio and the corresponding dashed line gives the model predictions which are calculated using chemical equilibrium grids generated using the NASA Gibbs minimization chemical equilibrium applications code (see Fegley & Lodders 1994; Fegley et al. 1996; Lodders 1999; Lodders & Fegley 2002; Lodders 2002; Lodders & Fegley 2006; Visscher et al. 2006; Lodders 2010; Visscher et al. 2010; Visscher 2012; Moses et al. 2013) at solar metallicity and C/O. The retrieved values are uniform with altitude and so show no variation with pressure, while the model predictions are calculated along the retrieved thermal profile (see Section 4.1) and so do show variations with pressure. The rapid decrease in the model mixing ratios of H₂O, H₂S, and NH₃ above $\sim 10^{-2}$ bar is a result of these species condensing out of the gas phase into water ice, ammonia ice, and NH₄SH (solid). The rapid increase in the mixing ratio of NH₃ above $10^{-3.2}$ bar is a result of the slight temperature reversal at the top of the thermal profile that is likely not physical (see Section 4.1).

The mixing ratio values of both H₂O and CH₄ indicate they are the most abundant species in the atmosphere and they agree well with the predictions. The NH₃ mixing ratio is 0.6 dex

lower than the model predicts at the nominal pressure of 1 bar, while the mixing ratios of CO and CO₂ are orders of magnitude higher at 1 bar. All three of these mismatches can be ascribed to disequilibrium chemistry due to vertical mixing in the atmosphere (Fegley et al. 1996; Saumon et al. 2000; Hubeny & Burrows 2007a). We defer a discussion of this disequilibrium chemistry to Section 4.5 where we attempt to measure the vigor of this mixing using the retrieved mixing ratios and a 1D chemical kinetics forward modeling framework. Finally, the mixing ratio of H₂S is 0.4 dex ($2.5\times$) higher than the model predicts.

4.4. Physical Properties: M , R , L_{bol} , g , and T_{eff}

The marginalized posterior distributions for M and R are shown in Figure 4. The M and R posterior samples can be used to calculate the posterior distribution for surface gravity ($g = MG/R^2$) and so the distribution of $\log(g)$ [cm s^{-2}] is also shown in Figure 4. The bolometric flux F_{bol} distribution can be calculated by integrating model spectra over all wavelengths. To account for light emerging at wavelengths shorter than $0.96 \mu\text{m}$ and longer than $12.0 \mu\text{m}$, we linearly interpolated the model from $0.96 \mu\text{m}$ to zero flux at zero wavelength and then extended the model to $\lambda = \infty$ using a Rayleigh–Jeans tail where $f_{\lambda, \text{RJ}} \propto \lambda^{-4}$; the constant of proportionality is calculated using the flux density of the last model wavelength. The bolometric luminosity is then given by $L_{\text{bol}} = 4\pi d^2 F_{\text{bol}}$, where d is the retrieved distance to the object, which results in the posterior distribution of $\log(L_{\text{bol}}/\mathcal{L}_{\odot}^{\text{N}})$ shown in Figure 4. Finally, we compute the effective temperature distribution shown in Figure 4 using the L_{bol} and R values and the Stefan–Boltzmann law,

$$T_{\text{eff}} = \left(\frac{L_{\text{bol}}}{4\pi\sigma R^2} \right)^{\frac{1}{4}}. \quad (7)$$

The retrieved mass of WISE 0359–54 is $10.4^{+1.5}_{-1.1} \mathcal{M}_{\text{Jup}}^{\text{N}}$, where $\mathcal{M}_{\text{Jup}}^{\text{N}}$ is the nominal Jupiter mass (assuming $G = 6.67430 \times 10^{-11} \text{ m}^3 \text{ kg}^{-1} \text{ s}^{-2}$, Mamajek et al. 2015). This value falls at the lower end of the $\sim 9\text{--}31 \mathcal{M}_{\text{Jup}}^{\text{N}}$ range reported in Beiler et al. (2023), who used the observed bolometric luminosity of WISE 0359–54, an assumed age range of 1–10 Gyr, and the Sonora Bobcat solar metallicity evolutionary models (Marley et al. 2021) to estimate the mass of WISE 0359–54.

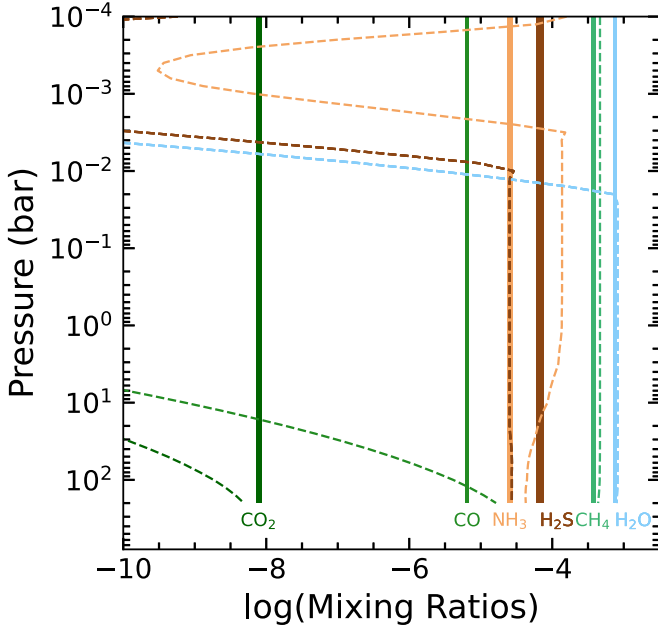


Figure 5. Retrieved uniform-with-altitude median mixing ratios with 1σ central credible interval (shaded) for H_2O , CH_4 , CO , CO_2 , NH_3 , and H_2S for WISE 0359–54 from the five-knot retrieval. Also shown are the predicted thermochemical equilibrium mixing ratios (dashed).

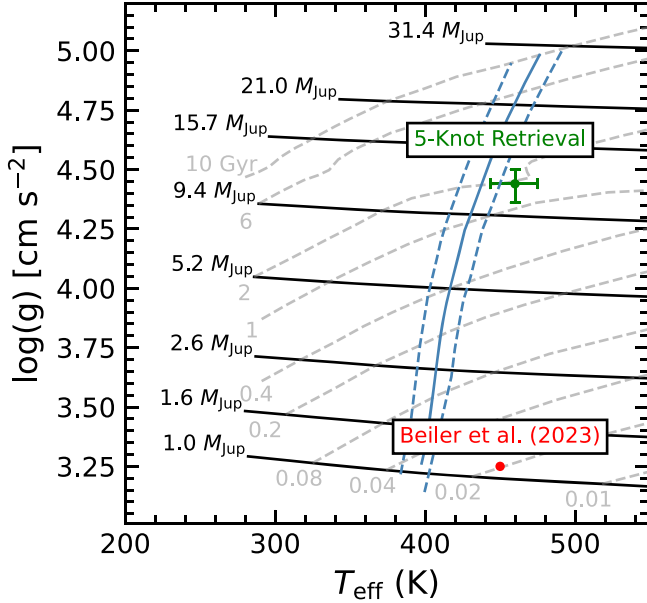


Figure 6. Evolution of Bobcat Sonora solar metallicity cloudless brown dwarfs in the effective temperature surface gravity plane (Marley et al. 2021). The black lines are cooling tracks for brown dwarfs with masses of 31.4, 21, 15.7, 9.4, 5.2, 2.6, 1.6, and $1 M_{\text{Jup}}^{\text{N}}$, while the gray lines are isochrones for ages of 10, 6, 2, 1, 0.4, 0.2, 0.08, 0.04, 0.02, and 0.01 Gyr. The loci of points with bolometric luminosities equal to that of WISE 0359–54 for ages between 0.1 and 10 Gyr are shown as the solid near-vertical lines while the $\pm 1\sigma$ uncertainties on the bolometric luminosities are shown as dotted lines. The blue dot shows the T_{eff} and $\log(g)$ value calculated using the five-knot retrieved results with the horizontal and vertical error bar representing 1σ interval for T_{eff} and $\log(g)$, respectively. The red dot is the best-fit Sonora Bobcat model in Beiler et al. (2023).

The retrieved radius is found to be $0.94 \pm 0.02 \mathcal{R}_{eJ}^{\text{N}}$, where $\mathcal{R}_{eJ}^{\text{N}}$ is Jupiter’s nominal equatorial radius of 7.1492×10^7 m (Mamajek et al. 2015). This is consistent with the value reported by Beiler et al. (2023), who used the observed

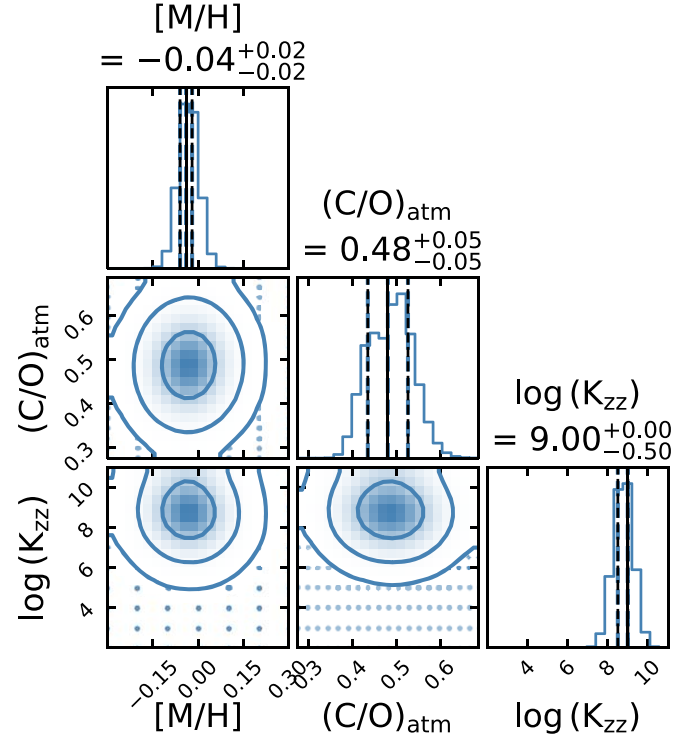


Figure 7. Corner plot showing the constraints on metallicity $[\text{M}/\text{H}]$, $(\text{C}/\text{O})_{\text{atm}}$, and K_{zz} obtained by fitting the retrieved gaseous abundances of CH_4 , CO , NH_3 , H_2O , and CO_2 with a grid of disequilibrium chemistry forward models. The grid of disequilibrium chemistry forward models uses the retrieved five-knot $T(P)$ profile constraint as an input and calculates the chemical abundance profiles across a large range of metallicity, $(\text{C}/\text{O})_{\text{atm}}$, and K_{zz} . Gaseous abundances obtained in the five-knot retrieval were used for this analysis.

bolometric luminosity of WISE 0359–54, an assumed age range of 1–10 Gyr, and the Sonora Bobcat solar metallicity evolutionary models (Marley et al. 2021) to find $0.94^{+0.074}_{-0.057} \mathcal{R}_{eJ}^{\text{N}}$ from a Monte Carlo simulation.

The bolometric luminosity of $\log(L_{\text{bol}}/\mathcal{L}_{\odot}^{\text{N}}) = -6.43^{+0.05}_{-0.06}$ is similar to the value of $\log(L_{\text{bol}}/\mathcal{L}_{\odot}^{\text{N}}) = -6.400 \pm 0.025$ reported by Beiler et al. (2023).

The retrieved surface gravity is $\log g = 4.46^{+0.06}_{-0.04}$ [cm s^{-2}] and the retrieved effective temperature is $T_{\text{eff}} = 458^{+15}_{-15}$ K. Figure 6 shows cloudless evolutionary models in the effective temperature/surface gravity plane with the position of WISE 0359–54 indicated. The loci of points with bolometric luminosities equal to that of WISE 0359–54 for ages between 0.1 and 10 Gyr is shown as a near-vertical line. The discrepancy between the two is most likely a result of the fact that the model does not extend to infinite wavelengths and thus our bolometric flux is systematically low. Also plotted is the best-fit effective temperature and surface gravity from Beiler et al. (2023), who used a custom grid of Sonora Cholla models (Karalidi et al. 2021) that includes an additional parameter K_{zz} , the vertical eddy diffusion coefficient. The Beiler et al. (2023) surface gravity is uncomfortably low, resulting in an age estimate of ~ 20 Myr. Our retrieved values give an age of ~ 2 Gyr, which is more consistent with the age estimates of the field population of warmer brown dwarfs (Dupuy & Liu 2017; Best et al. 2024).

4.5. Constraints on the Eddy Diffusion Parameter— K_{zz}

Vertical atmospheric dynamics can significantly alter the photospheric abundance of gases like CH_4 , NH_3 , CO , and CO_2

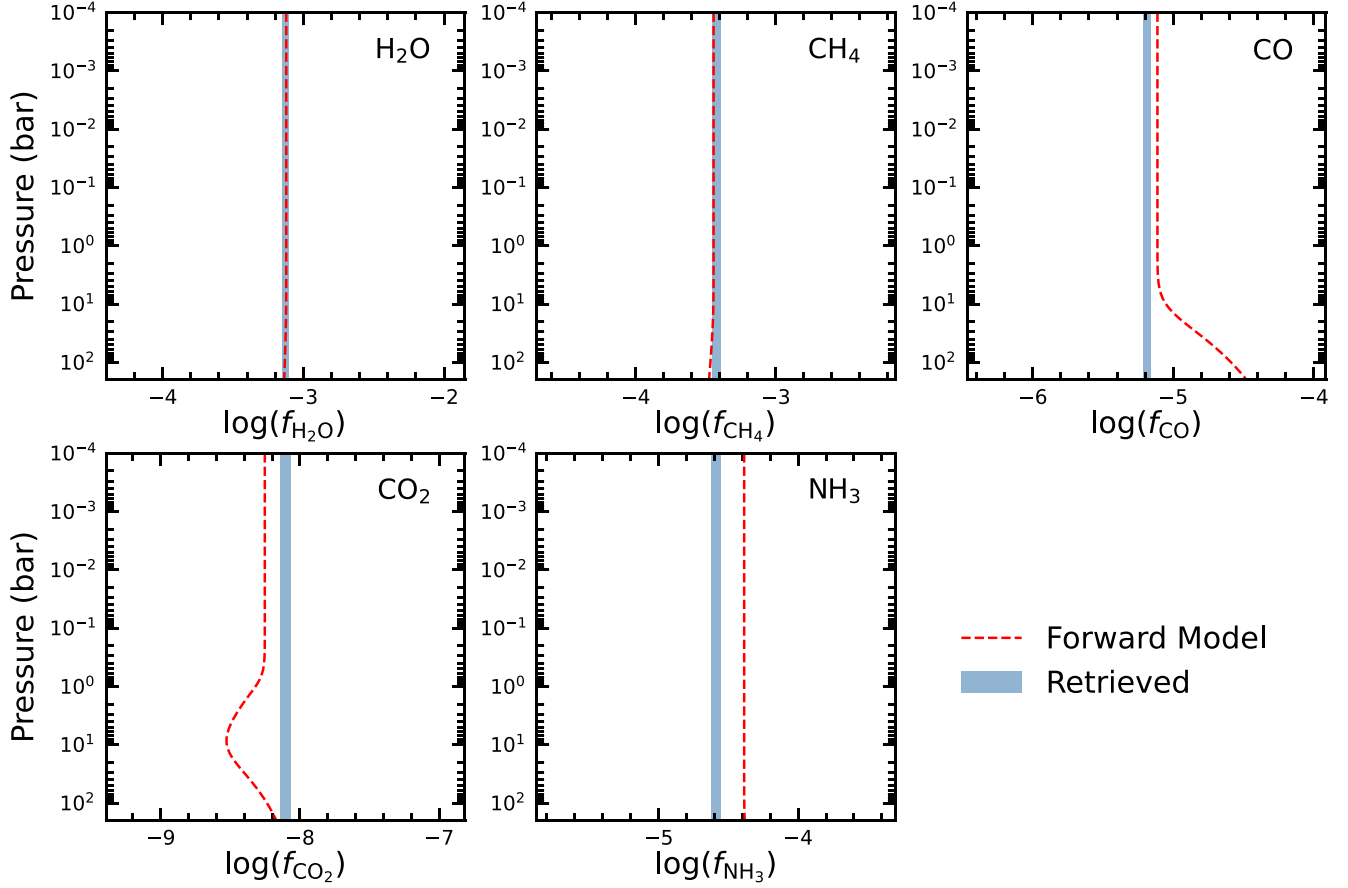


Figure 8. Comparison of the abundances in the best-fit disequilibrium chemistry forward model from `Photochem` with the retrieved abundances from the five-knot thermal profile. Retrieved volume mixing ratios of CH_4 , CO , NH_3 , H_2O , and CO_2 are shown with blue shaded regions (representing 1σ central credible interval) in each panel, whereas the red lines show the profiles from the best-fit forward model.

by dredging them up from the hotter, deeper atmosphere across several pressure scale heights. Exactly how much of the photospheric abundances are disturbed away from thermochemical equilibrium depends on the vigor of vertical mixing in the atmosphere of these objects (Fegley & Lodders 1994; Hubeny & Burrows 2007b; Visscher & Moses 2011; Zahnle & Marley 2014; Phillips et al. 2020; Karalidi et al. 2021; Mukherjee et al. 2022; Lacy & Burrows 2023; Lee et al. 2023). The strength of vertical mixing is often quantified using the vertical eddy diffusion parameter— K_{zz} . The K_{zz} parameter quantifies the rate of overturning motion occurring in the atmosphere and a higher K_{zz} represents more vigorous vertical mixing. But K_{zz} has remained uncertain (even in the solar system giants) by several orders of magnitude until now mainly because of the lack of access to high signal-to-noise-ratio spectra of brown dwarfs in the infrared, which can facilitate very precise constraints on atmospheric chemical abundances. The very precise constraints on the abundances of various gases obtained in this work make it a perfect target to constrain K_{zz} in its deep atmosphere.

In order to obtain constraints on K_{zz} from our retrieved gas abundances, we use the chemical kinetics model `Photochem` (Wogan et al. 2023). We use the median retrieved five-knot thermal profile as an input to the chemical kinetics model along with the median $\log(g)$ constraints obtained by our five-knot retrieval model. Using these inputs, we generate a grid of chemical forward models with `Photochem` by varying three key parameters that can influence the chemistry of brown

dwarfs—atmospheric metallicity, atmospheric $(\text{C}/\text{O})_{\text{atm}}$ ratio, and K_{zz} . For a given $(\text{C}/\text{O})_{\text{atm}}$, we remove about 20% of the O from the gas phase assuming it is used up in condensates in the deeper atmosphere. Our chemical forward model grid samples metallicities from subsolar to supersolar values between -0.3 and $+0.3$ with an increment of 0.1 dex except between -0.2 and $+0.1$, for which the increment is even smaller at 0.02 dex. We also vary the $(\text{C}/\text{O})_{\text{atm}}$ ratio from subsolar to supersolar values of 0.5 to $1.5 \times (\text{C}/\text{O})_{\odot}$, where the $(\text{C}/\text{O})_{\odot}$ is assumed to be 0.458. We vary $\log(K_{zz})$ from 2 to 11 with an increment of 1 except between the values of 6 to 10 where we include a finer sampling of 0.5. These K_{zz} values are in square centimeters per second.

We use the extensive grid of chemical forward models to fit the retrieved abundances with the model abundance profiles of CH_4 , CO , CO_2 , H_2O , and NH_3 at a pressure of 0.1 bar. We chose this pressure because it is smaller than the minimum quench pressures expected for these gases for the range of K_{zz} used in this work. For each forward model, we define a combined χ^2 using

$$\chi^2 = \sum_X \left(\frac{X_{\text{ret}} - X_{\text{model}}(0.1\text{bar})}{\sigma_{\text{ret}}^X} \right)^2, \quad (8)$$

where X_{ret} is the retrieved abundance of gas X , $X_{\text{model}}(0.1\text{bar})$ is the abundance of the same gas at 0.1 bar in the forward model grid, and σ_{ret}^X is the retrieved uncertainty on the abundance of gas X . We calculate the χ^2 of all our chemical

models using this formulation and then produce a corner plot for the sampled parameter points in our grid using $w = e^{-\chi^2/2}$ as weight for each sampled grid point.

Figure 7 shows this corner plot depicting our constraints on the atmospheric metallicity, $(C/O)_{\text{atm}}$ ratio, and K_{zz} obtained from the $T(P)$ profile and abundances retrieved using the five-knot modeling setup. The best-fit forward model abundance profiles for CH_4 , CO , CO_2 , H_2O , and NH_3 along with the retrieved abundances are shown in Figure 8. This analysis finds that the atmospheric metallicity of the object is very slightly subsolar and the $(C/O)_{\text{atm}}$ ratio is ~ 0.48 .

The best-fit K_{zz} value is found to be $10^9 \text{ cm}^2 \text{ s}^{-1}$, which is relatively large compared to previous estimates of K_{zz} in the atmospheres of cool brown dwarfs (Miles et al. 2020). Figure 8 shows that CH_4 and CO quench at ~ 10 bars in this best-fit case. This best-fit K_{zz} value is slightly inconsistent with the K_{zz} versus T_{eff} trend observed in Miles et al. (2020), where K_{zz} values continue to be low at $T_{\text{eff}} > 400$ K but show a dramatic rise when $T_{\text{eff}} < 400$ K. Mukherjee et al. (2022) used atmospheric forward models with a self-consistent treatment of disequilibrium chemistry to theoretically explain this trend as a result of gases quenching in deep “sandwiched” radiative zones with low K_{zz} in objects with $500 \text{ K} < T_{\text{eff}} < 1000$ K. The models showed that objects colder than 500 K tended to have gases quenched in their deep convective zones and are expected to show higher K_{zz} values representative of convective mixing. This theoretical trend was also found to have a significant gravity dependence in Mukherjee et al. (2022) where objects with $\log(g) < 4.5$ were expected to show convective zone quenching of gases across $400 \text{ K} < T_{\text{eff}} < 1000$ K.

Given that our five-knot retrievals show that our target has a T_{eff} of 458_{-15}^{+15} K and $\log(g)$ of $4.46_{-0.04}^{+0.06}$, our finding of a high K_{zz} makes it consistent with the trend predicted in Mukherjee et al. (2022). Therefore, it is likely that we are probing the deep convective zone K_{zz} in this object and not the radiative zone or “sandwiched” radiative zone K_{zz} , as expected from self-consistent forward model trends. The maximum K_{zz} in the deep convective atmosphere of a brown dwarf with T_{eff} of 458 K and $\log(g) = 4.46$ is $4.55 \times 10^{10} \text{ cm}^2 \text{ s}^{-1}$, calculated using Equation (4) in Zahnle & Marley (2014). This maximum K_{zz} in the convective zone is achieved when the entire energy flux from the interior is only carried out through convection in the deep atmosphere. However, in reality the interior energy flux is expected to be only partly carried out through convective transport and partly by radiative energy transport. In that case, the K_{zz} in the convective atmosphere is expected to be lower than this upper limit. Figure 8 also shows that our model-fitting approach fits the abundances of all these gases quite satisfactorily except for NH_3 . This might be suggestive of a slightly lower N/H ratio in the object than the scaled solar N/H ratio.

4.6. Sensitivity to Thermal Profile Model

In order to quantify whether our choice of thermal profile model impacts the resulting mixing ratios, we ran a second retrieval using the parametric thermal profile model described in (Madhusudhan & Seager 2009, hereafter M&S). In this model, the atmosphere is divided into three layers, for which the temperature and pressure are related by

$$P_0 < P < P_1 = P_0 e^{\alpha_1(T-T_0)^{1/2}} \text{ (Layer 1),} \quad (9)$$

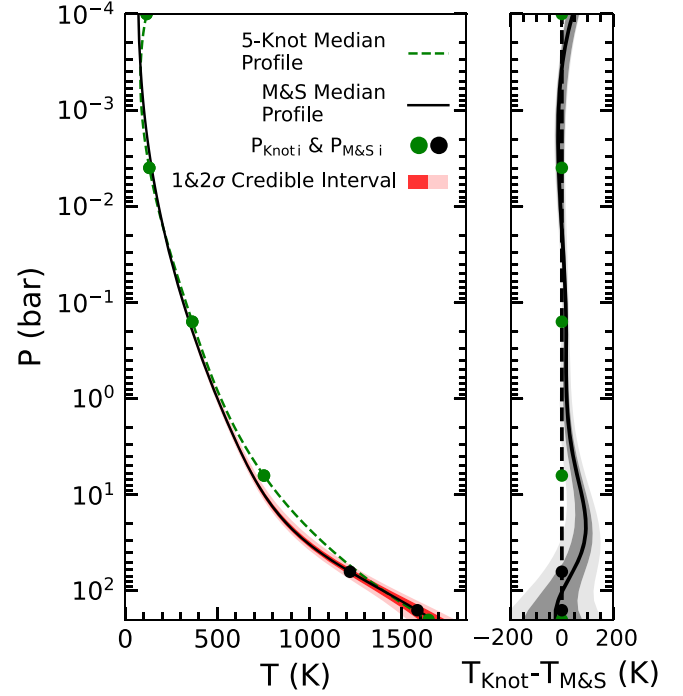


Figure 9. Left panel: shows the comparison between the two retrieved thermal profiles, where the black solid curve is the median M&S thermal profile, the red region shows the 1σ and 2σ confidence intervals around the median profile, and the green curve is the five-knot median thermal profile. Right panel: shows the difference between the five-knot and the M&S median profile, and the 1σ and 2σ central credible intervals, respectively.

$$P_1 < P < P_2 = P_2 e^{\alpha_2(T-T_2)^{1/2}} \text{ (Layer 2),} \quad (10)$$

$$P_3 < P = T_3 \text{ (Layer 3),} \quad (11)$$

where P_0 and T_0 are the pressure and temperature at the top of the atmosphere, respectively. We eliminate the possibility of a thermal inversion in the atmosphere by setting $P_2 = P_1$ and so we are left with five parameters: α_1 , α_2 , P_1 , P_3 , and T_3 , the priors of which are given in Table 1. In the Appendix, Figure 13 shows the marginalized posterior probability distributions for all 19 parameters and Table 3 gives the median and 1σ uncertainty for each of the parameters.

The left panel of Figure 9 shows a comparison between the retrieved five-knot thermal profile discussed in Section 4.1 and the M&S thermal profile while the right panel of Figure 9 shows the differences between the two. The profiles agree within the uncertainties except below a pressure of a bar where the five-knot profile is hotter by up to 100 K.

Figure 10 shows a comparison between the posterior distributions of the 12 parameters shown in Figure 4 ($f_{\text{H}_2\text{O}}$, f_{CH_4} , f_{CO} , f_{CO_2} , f_{NH_3} , $f_{\text{H}_2\text{S}}$, M , R , $(C/O)_{\text{atm}}$, $\log g$, L_{bol} , and T_{eff}) from the five-knot (blue) and the M&S (green) retrieval. Overall, the agreement between the distributions is good (see also Table 3), which suggests our results are not strongly dependent on the underlying thermal profile model. The largest differences are for the distributions of M and $\log(f_{\text{H}_2\text{S}})$ with fractional differences of the median values of -0.64 and -0.10 , respectively.

Figure 11 shows the retrieved median model spectrum from the M&S retrieval (black) along with the 1σ central credible interval (red) and the retrieved median model spectrum from the five-knot retrieval (green); the lower panel shows the

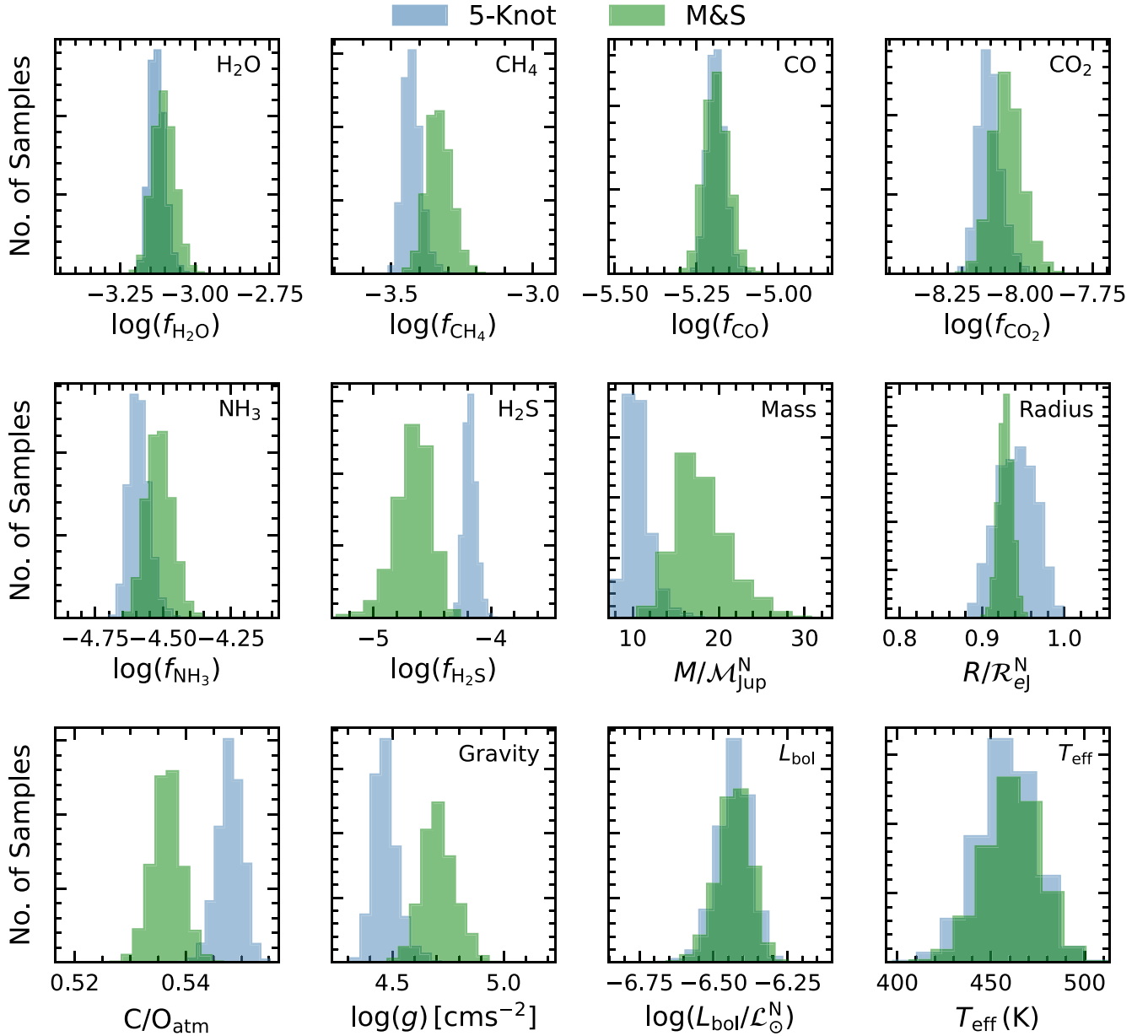


Figure 10. The posterior distributions retrieved for H_2O , CH_4 , CO , CO_2 , NH_3 , H_2S , mass, and radius alongside the calculated properties like $(\text{C}/\text{O})_{\text{atm}}$, gravity, L_{bol} , and T_{eff} from the five-knot (blue) and **M&S** (green) retrieval.

residual between the two models. Their five-knot profile predicts systematically higher fluxes in the J -, H -, and K -band opacity holes at 1.25, 1.6, and 2.1 μm and systematically lower fluxes between 5 and 7 μm . However, the median **M&S** retrieval predicts a higher flux in the Y band ($\sim 1 \mu\text{m}$); this may be a result of the increased retrieved abundance of Na and K (0.26 and 0.04 dex larger, respectively) which forces light that would otherwise escape at wavelengths shorter than 1 μm to instead emerge in the Y -band opacity hole.

We chose nested sampling to sample posterior values due to its inherent ability to estimate the evidence, $p(\mathbf{D})$. We can compute the posterior odds ratio between the five-knot model and the **M&S** model as

$$\frac{p(\text{five-knot}|\mathbf{D})}{p(\text{M\&S}|\mathbf{D})} = \frac{p(\text{five-knot})}{p(\text{M\&S})} \frac{p(\mathbf{D}|\text{five-knot})}{p(\mathbf{D}|p(\Theta_{\text{M\&S}}))}, \quad (12)$$

where the first term on the right-hand side is known as the prior odds and the last term on the right-hand side is known as the Bayes factor. Assuming the prior odds ratio is unity, the posterior odds is simply given by the Bayes factor

$$B_{\text{m}} = \frac{p(\mathbf{D}|p(\Theta_{\text{five knot}}))}{p(\mathbf{D}|p(\Theta_{\text{M\&S}}))}. \quad (13)$$

With $\ln p(\mathbf{D})$ values of 23540.66 ± 0.37 and 23560.97 ± 0.36 for the five-knot and **M&S** retrievals, respectively, we calculated a Bayes factor of 6.65×10^8 . Based on the Jeffreys' scale (Jeffreys 1998), this value suggests that the **M&S** thermal profile is strongly preferred over the five-knot profile. We can convert this value to an equivalent “ σ ” significance as described in Benneke & Seager (2013) and find a value of 6.69σ .

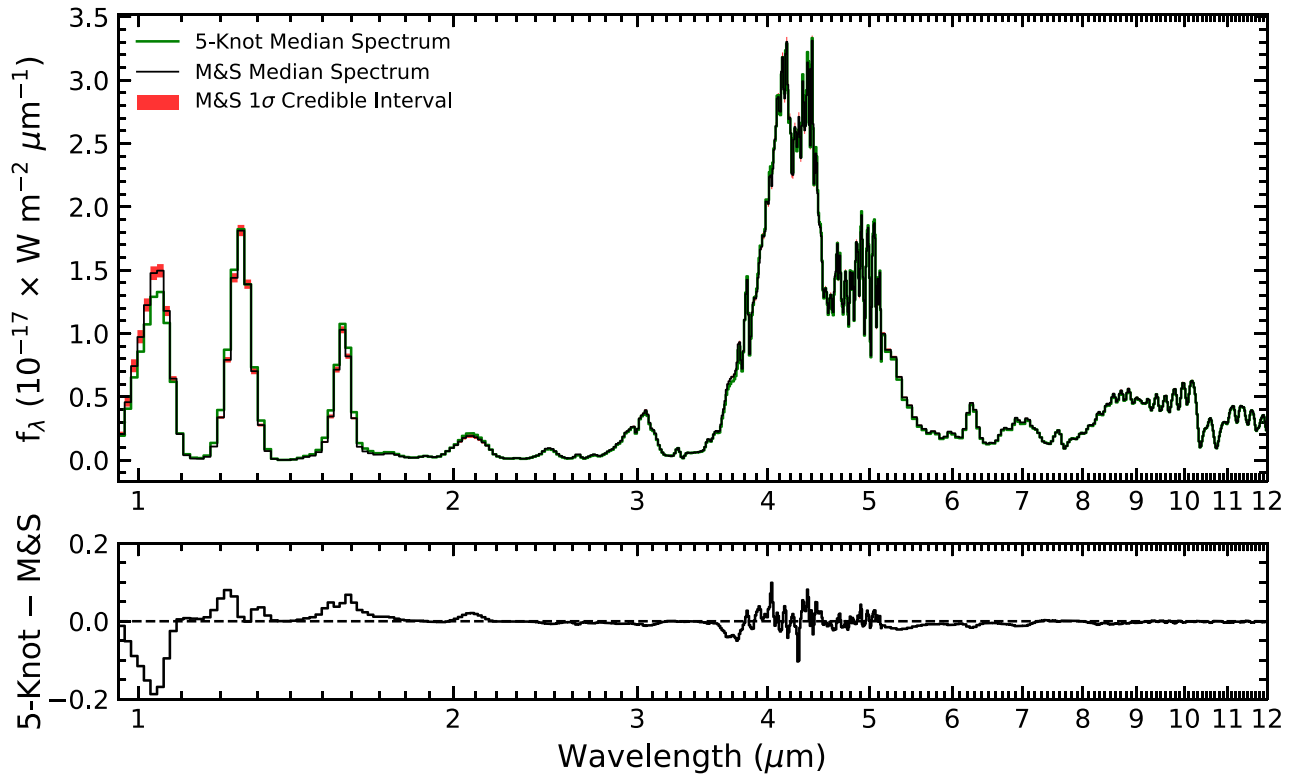


Figure 11. The top panel of the figure shows the retrieved median spectrum from the [M&S](#) retrieval in black and the retrieved median spectrum from five-knot retrieval in green for WISE 0359–54 spectrum covering 0.96–12 μm . The red region shows the 1σ region around the [M&S](#) median spectrum. The bottom panel of the figure shows the residual spectrum calculated by taking the difference between the retrieved [M&S](#) median spectrum and the retrieved five-knot median spectrum.

5. Summary

In this work, we present an atmospheric retrieval analysis of the Y0 brown dwarf WISE 0359–54 using the low-resolution 0.96–12 μm JWST spectrum obtained using NIRSpec and MIRI. The cloudless retrieval was performed using the Brewster retrieval framework. We retrieved volume number mixing ratios for nine gases: H_2O , CH_4 , CO , CO_2 , NH_3 , H_2S , K , Na , and PH_3 . These retrieved mixing ratios are 3–5 \times more precise than the previous work done using the HST WFC3 data (Zalesky et al. 2019). Since we were able to constrain all the major carbon- and oxygen-bearing molecules, we found $(\text{C}/\text{O})_{\text{atm}}$ to be 0.548 ± 0.002 . Apart from constraining the chemical composition, we also found an order-of-magnitude improvement in the precision of the retrieved thermal profile, which can be attributed to the broad-wavelength coverage of the JWST data.

Using the retrieved thermal profile and the calculated surface gravity, we generated a grid of forward models with varying metallicity $[\text{M}/\text{H}]$, $(\text{C}/\text{O})_{\text{atm}}$, and eddy diffusion coefficient (K_{zz}), which tells the atmospheric mixing vigor. Comparing these generated models with our retrieved mixing ratios of H_2O , CH_4 , CO , CO_2 , and NH_3 , we found strong evidence of vertical mixing in the atmosphere of WISE 0359–54 with a value of $K_{zz} = 10^9 \text{ [cm}^2 \text{ s}^{-1}\text{]}$.

Finally, to test the sensitivity of our results to our five-knot thermal profile model, we performed another retrieval using the [M&S](#) thermal profile model. We found that the mixing ratios from both thermal profile models yield similar results (with the exception of $f_{\text{H}_2\text{S}}$, which is -0.10 dex lower) and that the retrieved thermal profile is similar except near the 5 bar pressure level, where it is ~ 100 K hotter. Taken together, these results underscore the power that the JWST has to study the atmospheres of the coolest brown dwarfs.

Acknowledgments

This work is based [in part] on observations made with the NASA/ESA/CSA JWST. These observations are associated with program #2302.

This research has made use of the SIMBAD database, operated at CDS, Strasbourg, France.

We would also like to thank Jacqueline K. Faherty and Channon Visscher for their valuable insight into the retrieved results and the workings of the chemistry in such cold objects.

Software: Corner (Foreman-Mackey 2016), Matplotlib (Hunter 2007), NumPy (Harris et al. 2020).

Appendix

Figures 12 and 13 show the marginalized posterior probability distributions for all 19 retrieved parameters. Table 3 shows the

retrieved median parametric values with their respective 1σ uncertainties from the five-knot and M&S retrieval. The last column in Table 3 shows the fractional difference between both the retrievals.

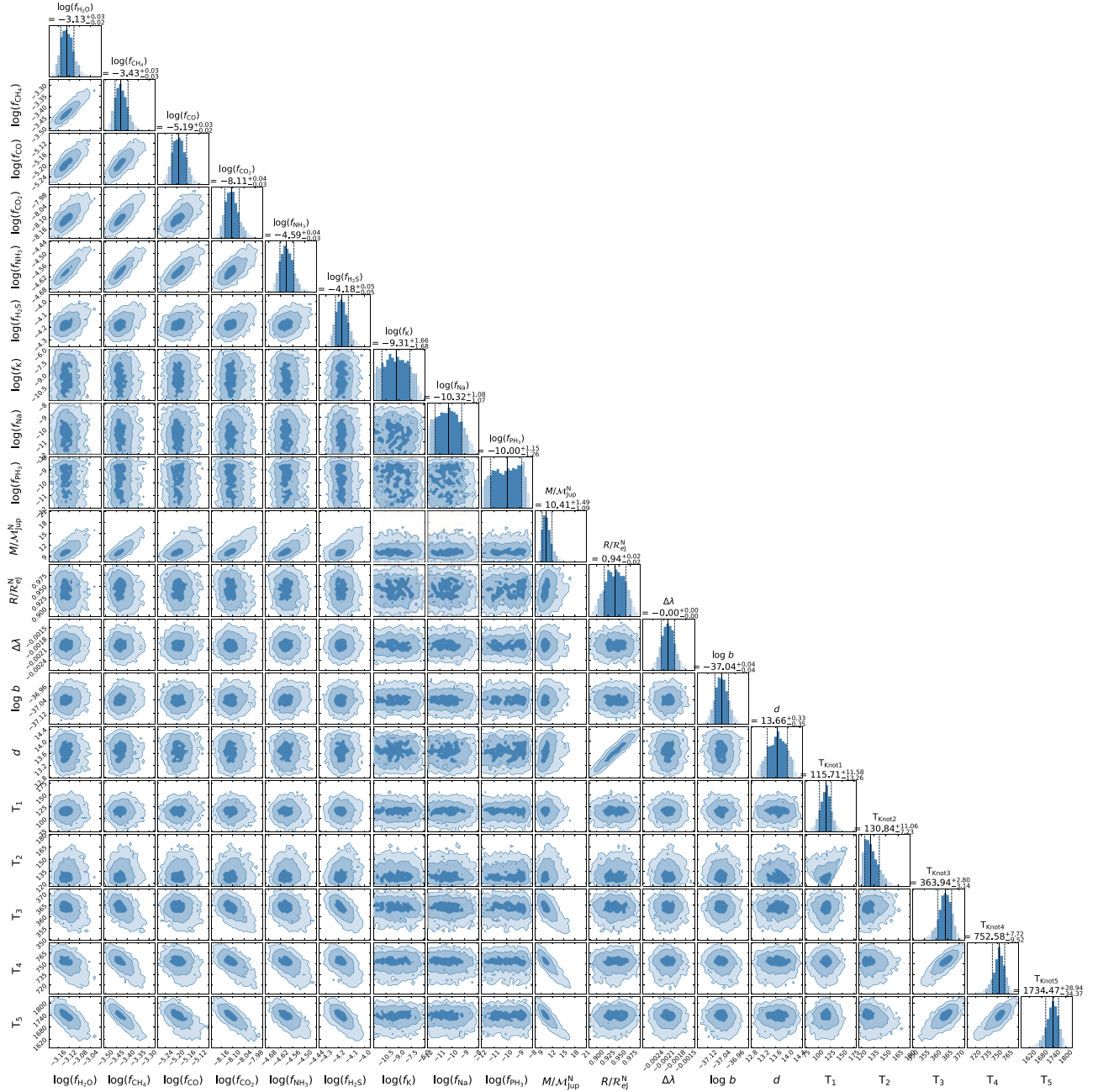


Figure 12. Marginalized posterior probability distributions for each parameter from the five-knot retrieval for WISE 0359–54. The first nine parameters represent the retrieved mixing ratios for H₂O, CH₄, CO, CO₂, NH₃, H₂S, K, Na, and PH₃, followed by mass and radius. The parameters $\Delta\lambda$ and $\log b$ are nuisance parameters, d is the distance to the object, and the last five parameters are the retrieved temperature knots. The values above the 1D histograms represent the parametric median (50th percentile) values, with the errors representing the 1σ central credible interval (16th and 84th percentiles) values. The different shades in the 1D and 2D histograms represent the 1σ , 2σ , and 3σ central credible intervals, respectively, with the darkest shade corresponding to 1σ .

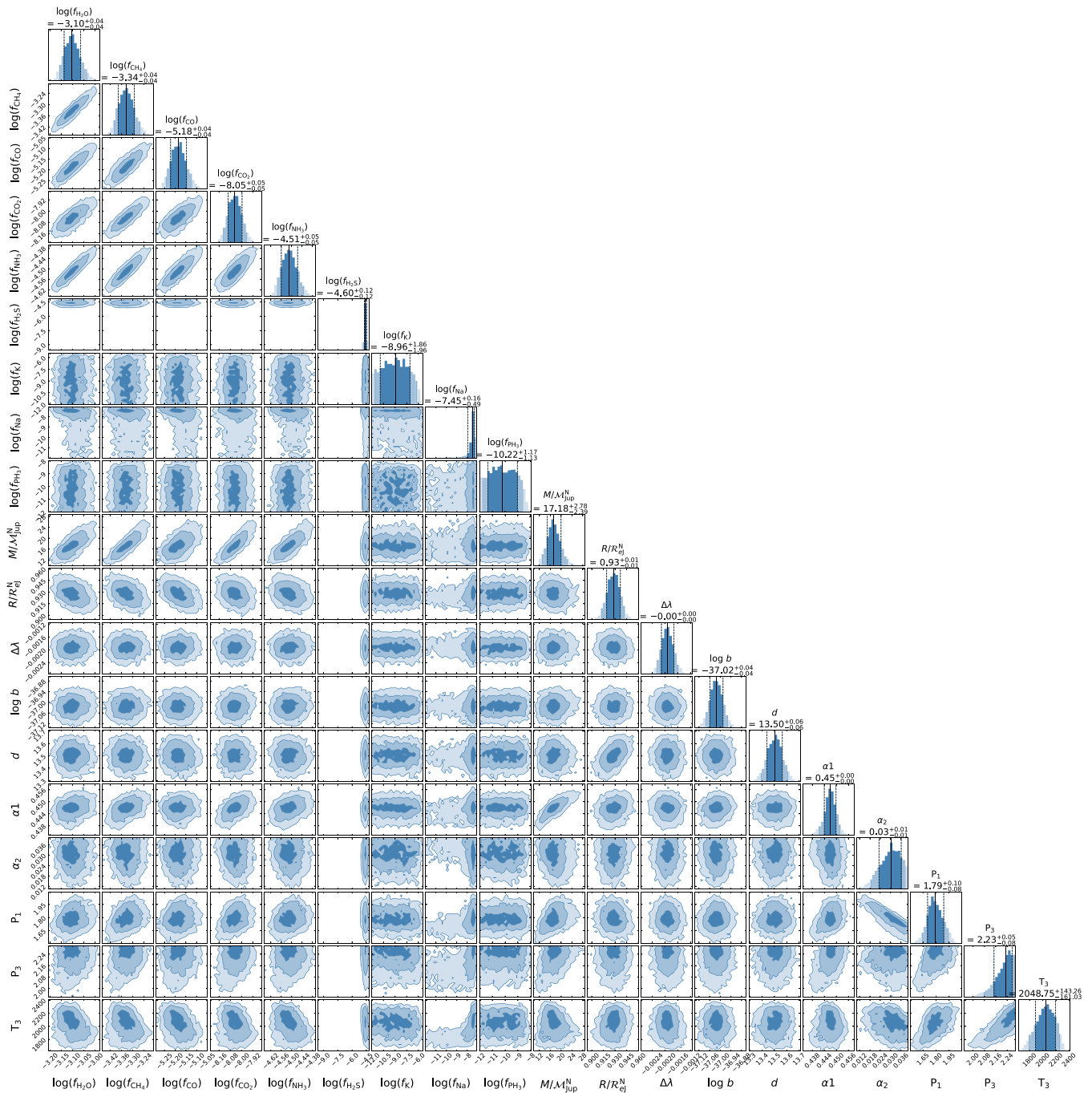


Figure 13. Marginalized posterior probability distributions for each parameter from the M&S retrieval for WISE 0359–54. The first nine parameters represent the retrieved mixing ratios for H₂O, CH₄, CO, CO₂, NH₃, H₂S, K, Na, and PH₃, followed by mass and radius. The parameters Δ and $\log b$ are nuisance parameters, d is the distance to the object, and the last five parameters are the retrieved temperature knots (points). The values above the 1D histograms represent the parametric median (50th percentile) values with the errors representing the 1σ central credible interval (16th and 84th percentiles) values. The different shades in the 1D and 2D histograms represent the 1σ , 2σ , and 3σ central credible intervals, respectively, with the darkest shade corresponding to 1σ .

Table 3
Posterior Parametric Values


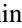


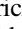
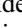


Parameter	Five-knot Retrieval ^a	M&S Retrieval ^a	Fractional Difference ^b
$\log(f_{\text{H}_2\text{O}})$	$-3.13^{+0.03}_{-0.02}$	$-3.10^{+0.04}_{-0.04}$	$0.01^{+0.01}_{-0.01}$
$\log(f_{\text{CH}_4})$	$-3.43^{+0.03}_{-0.03}$	$-3.34^{+0.04}_{-0.04}$	$0.03^{+0.01}_{-0.01}$
$\log(f_{\text{CO}})$	$-5.19^{+0.03}_{-0.02}$	$-5.18^{+0.04}_{-0.04}$	$0.00^{+0.01}_{-0.01}$
$\log(f_{\text{CO}_2})$	$-8.11^{+0.04}_{-0.03}$	$-8.05^{+0.05}_{-0.05}$	$0.01^{+0.01}_{-0.01}$
$\log(f_{\text{NH}_3})$	$-4.59^{+0.04}_{-0.03}$	$-4.51^{+0.05}_{-0.05}$	$0.02^{+0.01}_{-0.01}$
$\log(f_{\text{H}_2\text{S}})$	$-4.18^{+0.05}_{-0.05}$	$-4.60^{+0.12}_{-0.12}$	$-0.10^{+0.03}_{-0.03}$
$\log(f_{\text{K}})$	$-9.31^{+1.66}_{-1.68}$	$-8.96^{+1.86}_{-1.96}$	$0.03^{+0.23}_{-0.28}$
$\log(f_{\text{Na}})$	$-10.32^{+1.08}_{-1.07}$	$-7.45^{+0.16}_{-0.49}$	$0.26^{+0.08}_{-0.11}$
$\log(f_{\text{PH}_3})$	$-10.00^{+1.15}_{-1.26}$	$-10.22^{+1.17}_{-1.13}$	$-0.02^{+0.15}_{-0.17}$
$M/M_{\text{Jup}}^{\text{N}}$	$10.40^{+1.50}_{-1.10}$	$17.20^{+2.80}_{-2.40}$	$-0.64^{+0.30}_{-0.34}$
$R/R_{\text{ej}}^{\text{N}}$	$0.94^{+0.02}_{-0.02}$	$0.93^{+0.01}_{-0.01}$	$0.01^{+0.03}_{-0.03}$
$\Delta\lambda$	$0.00^{+0.00}_{-0.00}$	$0.00^{+0.00}_{-0.00}$	$0.04^{+0.13}_{-0.14}$
$\log b$	$-37.04^{+0.04}_{-0.04}$	$-37.02^{+0.04}_{-0.04}$	$0.00^{+0.00}_{-0.00}$
d	$-13.66^{+0.33}_{-0.35}$	$-13.50^{+0.02}_{-0.03}$	$0.01^{+0.01}_{-0.01}$
$T_{\text{Knot } 1}$	$115.71^{+11.58}_{-13.26}$
$T_{\text{Knot } 2}$	$130.84^{+11.06}_{-7.23}$
$T_{\text{Knot } 3}$	$363.94^{+2.80}_{-3.14}$
$T_{\text{Knot } 4}$	$752.58^{+7.72}_{-9.52}$
$T_{\text{Knot } 5}$	$1734.47^{+28.94}_{-34.37}$
α_1	...	$0.45^{+0.00}_{-0.00}$...
α_2	...	$0.03^{+0.01}_{-0.01}$...
P_1	...	$1.79^{+0.10}_{-0.08}$...
P_3	...	$2.23^{+0.06}_{-0.08}$...
T_1	...	$2048.75^{+143.26}_{-161.03}$...

Notes.

^a All mixing ratios are reported as the log of the volume mixing ratio (the amount of molecular gas out of the total amount of molecular gas), where the remainder of the gas is assumed to be H₂-He at a fixed solar ratio.

^b The difference between the five-knot and M&S retrieved posterior samples divided by the five-knot retrieved posterior samples.

ORCID iDs

Harshil Kothari  <https://orcid.org/0009-0009-4489-0192>
 Michael C. Cushing  <https://orcid.org/0000-0001-7780-3352>
 Ben Burningham  <https://orcid.org/0000-0003-4600-5627>
 Samuel A. Beiler  <https://orcid.org/0000-0002-6721-1844>
 J. Davy Kirkpatrick  <https://orcid.org/0000-0003-4269-260X>
 Adam C. Schneider  <https://orcid.org/0000-0002-6294-5937>
 Sagnick Mukherjee  <https://orcid.org/0000-0003-1622-1302>
 Mark S. Marley  <https://orcid.org/0000-0002-5251-2943>

References

Adams, A. D., Meyer, M. R., Howe, A. R., et al. 2023, *AJ*, 166, 192
 Asplund, M., Grevesse, N., Sauval, A. J., & Scott, P. 2009, *ARA&A*, 47, 481
 Barrado, D., Mollière, P., Patapis, P., et al. 2023, *Natur*, 624, 263
 Barshay, S. S., & Lewis, J. S. 1978, *Icar*, 33, 593
 Beer, R. 1975, *ApJL*, 200, L167
 Beiler, S. A., Cushing, M. C., Kirkpatrick, J. D., et al. 2023, *ApJL*, 951, L48
 Benneke, B., & Seager, S. 2013, *ApJ*, 778, 153
 Best, W. M. J., Sanghi, A., Liu, M. C., Magnier, E. A., & Dupuy, T. J. 2024, *ApJ*, 967, 115
 Bregman, J. D., Lester, D. F., & Rank, D. M. 1975, *ApJL*, 202, L55

Buchner, J., Georgakakis, A., Nandra, K., et al. 2014, *A&A*, 564, A125
 Burningham, B., Marley, M. S., Line, M. R., et al. 2017, *MNRAS*, 470, 1177
 Calamari, E., Faherty, J. K., Channon, V., et al. 2024, arXiv:2401.11038
 Center, O. S. 1987, Ohio Supercomputer Center, <http://osc.edu/ark:/19495/f5s1ph73>
 Center, O. S. 2016, Owens Supercomputer, <http://osc.edu/ark:/19495/hpc6h5b1>
 Chahine, M. T. 1968, *JOSA*, 58, 1634
 Chamberlain, J. W., & Hunten, D. M. 1987, Theory of Planetary Atmospheres. An Introduction to Their Physics and Chemistry, Vol. 36 (Cambridge, MA: Academic Press)
 Dupuy, T. J., & Liu, M. C. 2017, *ApJS*, 231, 15
 Faherty, J., Burningham, B., Gagné, J., et al. 2024, *BAAS*, 56, 101
 Fegley, B., & Lodders, K. 1994, *Icar*, 110, 117
 Fegley, Bruce, J., & Lodders, K. 1996, *ApJL*, 472, L37
 Feroz, F., Hobson, M. P., & Bridges, M. 2009, *MNRAS*, 398, 1601
 Foreman-Mackey, D. 2016, *JOSS*, 1, 24
 Foreman-Mackey, D., Conley, A., Meierjürgen Farr, W., et al. 2013, emcee: The MCMC Hammer, Astrophysics Source Code Library, ascl:1303.002
 Gardner, J. P., Mather, J. C., Clampin, M., et al. 2006, *SSRv*, 123, 485
 Gillett, F. C., Forrest, W. J., & Merrill, K. M. 1973, *ApJ*, 183, 87
 Harris, C. R., Millman, K. J., van der Walt, S. J., et al. 2020, *Natur*, 585, 357
 Hogg, D. W., Bovy, J., & Lang, D. 2010, arXiv:1008.4686
 Hood, C. E., Fortney, J. J., Line, M. R., & Faherty, J. K. 2023, *ApJ*, 953, 170
 Hood, C. E., Mukherjee, S., Fortney, J. J., et al. 2024, arXiv:2402.05345
 Hubeny, I., & Burrows, A. 2007a, *ApJ*, 669, 1248
 Hubeny, I., & Burrows, A. 2007b, *ApJ*, 659, 1458
 Hunter, J. D. 2007, *CSE*, 9, 90
 Jakobsen, P., Ferruit, P., Alves de Oliveira, C., et al. 2022, *A&A*, 661, A80
 Jeffreys, H. 1998, The Theory of Probability, Oxford Classic Texts in the Physical Sciences (Oxford: OUP), <https://books.google.com/books?id=vh9Act9rtzQC>
 Karalidi, T., Marley, M., Fortney, J. J., et al. 2021, *ApJ*, 923, 269
 Kirkpatrick, D. J., Gelino, C. R., Cushing, M. C., et al. 2012, *ApJ*, 753, 156
 Kirkpatrick, J. D., Gelino, C. R., Faherty, J. K., et al. 2021, *ApJS*, 253, 7
 Lacy, B., & Burrows, A. 2023, *ApJ*, 950, 8
 Lee, E. K. H., Tan, X., & Tsai, S.-M. 2023, *MNRAS*, 523, 4477
 Lew, B. W. P., Roellig, T., Batalha, N. E., et al. 2024, *AJ*, 167, 237
 Line, M. R., Fortney, J. J., Marley, M. S., & Sorahana, S. 2014, *ApJ*, 793, 33
 Lodders, K. 1999, *ApJ*, 519, 793
 Lodders, K. 2002, *ApJ*, 577, 974
 Lodders, K. 2010, *ASSP*, 16, 379
 Lodders, K., & Fegley, B. 2002, *Icar*, 155, 393
 Lodders, K., & Fegley, B. 2006, Chemistry of Low Mass Substellar Objects (Berlin: Springer), 1
 Lueber, A., Kitzmann, D., Bowler, B. P., Burgasser, A. J., & Heng, K. 2022, *ApJ*, 930, 136
 Luhman, K. L., Tremblin, P., de Oliveira, C. A., et al. 2024, *AJ*, 167, 5
 Madhusudhan, N., & Seager, S. 2009, *ApJ*, 707, 24
 Mamajek, E. E., Prsa, A., Torres, G., et al. 2015, arXiv:1510.07674
 Marley, M. S., Saumon, D., Visscher, C., et al. 2021, *ApJ*, 920, 85
 Miles, B. E., Skemer, A. J. I., Morley, C. V., et al. 2020, *AJ*, 160, 63
 Moses, J. I., Line, M. R., Visscher, C., et al. 2013, *ApJ*, 777, 34
 Mukherjee, S., Fortney, J. J., Batalha, N. E., et al. 2022, *ApJ*, 938, 107
 Mukherjee, S., Fortney, J. J., Morley, C. V., et al. 2024, *ApJ*, 963, 73
 Phillips, M. W., Tremblin, P., Baraffe, I., et al. 2020, *A&A*, 637, A38
 Rieke, G. H., Ressler, M. E., Morrison, J. E., et al. 2015, *PASP*, 127, 665
 Rowland, M. J., Morley, C. V., & Line, M. R. 2023, *ApJ*, 947, 6
 Saumon, D., Geballe, T. R., Leggett, S. K., et al. 2000, *ApJ*, 541, 374
 Schneider, A. C., Cushing, M. C., Kirkpatrick, J. D., et al. 2015, *ApJ*, 804, 92
 Spagle, J. S. 2020, *MNRAS*, 493, 3132
 Tannock, M. E., Metchev, S., Hood, C. E., et al. 2022, *MNRAS*, 514, 3160
 Toon, O. B., McKay, C. P., Ackerman, T. P., & Santhanam, K. 1989, *JGR*, 94, 16287
 Visscher, C. 2012, *ApJ*, 757, 5
 Visscher, C., & Moses, J. I. 2011, *ApJ*, 738, 72
 Visscher, C., Lodders, K., & Fegley, B., Jr. 2006, *ApJ*, 648, 1181
 Visscher, C., Lodders, K., & Fegley, B. J. 2010, *ApJ*, 716, 1060
 Vos, J. M., Burningham, B., Faherty, J. K., et al. 2023, *ApJ*, 944, 138
 Wogan, N. F., Catling, D. C., Zahnle, K. J., & Lupu, R. 2023, *PSJ*, 4, 169
 Zahnle, K. J., & Marley, M. S. 2014, *ApJ*, 797, 41
 Zalesky, J. A., Line, M. R., Schneider, A. C., & Patience, J. 2019, *ApJ*, 877, 24